Earth Planet. Sci. Lett. 691 (2026) 120235



Contents lists available at ScienceDirect

Earth and Planetary Science Letters

journal homepage: www.elsevier.com/locate/epsl





Rock physics modeling reveals large uncertainty in midcrustal liquid water on Mars

Mufan Zha [a,*], Per Avseth [b], Paul Sava [a]

[a] Center for Wave Phenomena, Department of Geophysics, Colorado School of Mines, Golden, 80401, CO, USA
[b] Dig Technology, Oslo, Norway

ARTICLE INFO

Editor : Dr O Mousis

Keywords:
Mars
Liquid water
Rock physics
Bayesian inversion
InSight seismology

ABSTRACT

How much liquid water resides in Mars' mid-crust remains debated. Wright et al. (2024) inferred about 1–2 km of equivalent water layer at 11.5–20 km depth. That result, however, was derived using a single rock-physics model and one specific configuration of elastic parameter inputs, which represent only one of many rock-physical possibilities. This limited scope motivates a comprehensive re-evaluation to test how the inferred water content depends on these foundational assumptions. We conduct a Bayesian rock-physics inversion that spans additional rock-physical theories and a collection of plausible elastic parameters, derived from observations reported in the literature. We find that the inferred water thickness depends strongly on the rock-physics and seismic input choices, from nearly 0 km to ~3.2 km. Considering model assumptions and data provenance, the most parsimonious but highly uncertain model-data combination yields an equivalent crustal water layer thickness near 0 km. These results indicate that current observations do not uniquely constrain mid-crustal liquid water on Mars and motivate the need for tighter seismic constraints and rock-physical measurements.

1. Introduction

Water on Mars has long been a topic of interest (Squyres, 1984; Nazari-Sharabian et al., 2020; Carr and Head, 2010). Numerous studies indicate that Mars was historically a wet planet, though much of this water has since been lost (Squyres, 1984; Kurokawa et al., 2014; Krasnopolsky, 2002). Hydrogen isotopic analysis of the atmosphere and martian meteorites, for example, suggests that Mars has lost a significant portion of its primordial water reservoir to space (Kurokawa et al., 2014). Atmospheric modeling indicates the loss of more than 1.3 km of water, expressed as a global-equivalent layer, over Martian history—chiefly through the reaction of water with iron and the subsequent hydrodynamic escape of hydrogen (Krasnopolsky, 2002). Multiple studies of Martian hydrated minerals indicate that a large amount of water — equivalent to a global layer hundreds of meters deep — is stored within or required to form these minerals (Wernicke and Jakosky, 2021; Scheller et al., 2021). The remaining water is now largely sequestered as polar ice. Recent radar sounding data estimates the south polar cap alone contains ~ 10^6 km^3 of water ice (Genova et al., 2024). Furthermore, radar evidence has been interpreted as subglacial lakes at the base of the polar caps, likely composed of brines (Orosei et al., 2018), although the same bright basal reflections can also be explained by thin-layer interference (Lalich et al., 2022). However, while these studies confirm abundant surface and polar ice and point to possible—though contested—subglacial water, whether a significant volume of Mars's historical water was sequestered deep within the crust, and if it can persist there as liquid today, remains a key unknown (Clifford and Parker, 2001).

Recent research suggests that a large amount of water may be present in the Martian mid-crust (Wright et al., 2024). Geophysical arguments from seismic soundings provide the first detailed velocity structure of the Martian crust, identifying a mid-crustal layer (11.5–20 km depth) with specific rock-physical properties (Knapmeyer-Endrun et al., 2021). Laboratory constraints from rock physics modeling demonstrate that these specific seismic velocities are consistent with a lithology of porous, fractured basalt, potentially saturated with liquid water or brines (Kilburn et al., 2022). Building on this, Wright et al. (2024) use rock-physical modeling to assess how much water could be trapped in the Mars mid-crust, inferring ~ 1–2 km of water spanning the entire planet.

Although that result is influential (Bernadet et al., 2025; Katayama and Akamatsu, 2024; Knapmeyer-Endrun et al., 2025), several limitations motivate a broader test. To assess the robustness of its conclusions, we test a comprehensive suite of distinct rock-physical model families: Hashin–Shtrikman (HS) (Avseth et al., 2020), Differential Effective Medium (DEM) (Berryman et al., 2002), Kuster–Toksöz (KT) (Kuster and Toksoz, 1974), and Voigt–Reuss–Hill (VRH)

* Corresponding author.
E-mail address: mufan_zha@mines.edu (M. Zha).

https://doi.org/10.1016/j.epsl.2026.120235
Received 1 April 2026; Received in revised form 7 July 2026; Accepted 13 July 2026
Available online 21 July 2026
0012-821X/© 2026 The Authors. Published by Elsevier B.V. This is an open access article under the CC BY-NC license (http://creativecommons.org/licenses/by-nc/4.0/).

Table 1
Rock physics theories.

	Dry frame	Fluid mixing	Fluid substitution
1	Berryman's Self-Consistent Model (SCM) Wright et al. (2024), Berryman (1980)	Voigt Voigt (1910)	Gassmann–Biot Gassmann (1951), Biot (1956), Mavko et al. (2020)
2	Berryman's Self-Consistent Model (SCM) Wright et al. (2024), Berryman (1980)	Hill Hill (1952)	Gassmann–Biot Gassmann (1951), Biot (1956), Mavko et al. (2020)
3	Hashin–Shtrikman (HS) Avseth et al. (2020), Hashin and Shtrikman (1963)	Voigt Voigt (1910)	Gassmann–Biot Gassmann (1951), Biot (1956), Mavko et al. (2020)
4	Hashin–Shtrikman (HS) Avseth et al. (2020), Hashin and Shtrikman (1963)	Hill Hill (1952)	Gassmann–Biot Gassmann (1951), Biot (1956), Mavko et al. (2020)
5	Differential Effective Medium (DEM) Berryman et al. (2002)	Voigt Voigt (1910)	—
6	Differential Effective Medium (DEM) Berryman et al. (2002)	Hill Hill (1952)	—
7	Kuster–Toksöz (KT) Kuster and Toksoz (1974)	—	—
8	Voigt–Reuss–Hill (VRH) Hill (1952)	—	—

Table 2
Elastic parameters used in inversion. References (Knapmeyer-Endrun et al., 2021; Duran et al., 2022; Carrasco et al., 2023; Joshi et al., 2023; Wieczorek et al., 2022; Lewis et al., 2019; Johnson et al., 2021) contributed the parameters averaged in the Wright et al. (2024) study.

	V_p km/s	σ_{V_p} km/s	V_s km/s	σ_{V_s} km/s	ρ_b kg/m^3	σ_b kg/m^3
Li et al. (2022)	3.8	1.0	2.2	0.4	—	—
Knapmeyer-Endrun et al. (2021)	—	—	2.3	0.3	—	—
Duran et al. (2022)	—	—	2.9	0.4	—	—
Carrasco et al. (2023)	4.15	0.4	2.25	0.25	—	—
Joshi et al. (2023)	—	—	2.45	0.15	—	—
Wieczorek et al. (2022), Lewis et al. (2019), Johnson et al. (2021)	—	—	—	—	2589	157
Wright et al. (2024)	4.1	0.2	2.5	0.3	2589	157
Drilleau et al. (2022)	4.7	0.3	2.7	0.1	—	—

(Voigt, 1910; Reuss, 1929; Hill, 1952) to evaluate the sensitivity of liquid water distribution to the specific assumptions of the rock-physical model. Although Berryman's Self-Consistent Model (SCM), adopted by Wright et al. (2024), incorporates geometries of inclusions, it can break down when their shear modulus is zero and at specific aspect ratios (Wright et al., 2024; Mavko et al., 2020), limiting exploration of the influence of crack geometry on the inferred distribution of water at crustal depth. Wright et al. (2024) also use Voigt fluid mixing (iso-strain), which represents complete phase segregation, although this phenomenon seems unlikely. Additionally, the V_p and V_s values used in the study represent averages from several studies (Wright et al., 2024; Knapmeyer-Endrun et al., 2021; Duran et al., 2022; Carrasco et al., 2023; Joshi et al., 2023; Wieczorek et al., 2022; Lewis et al., 2019; Johnson et al., 2021), which may influence the V_p/V_s ratio and bias the inferred crustal water content. Moreover, Wright et al. (2024) derive their single thickness estimate by substituting the marginal modes of porosity and saturation into $D_{\text{water}} = D_{\text{mid-crust}}\,\phi'\,S'_w$, rather than propagating the joint distribution of the two (their Fig. 1E) into the thickness—a joint distribution that strongly affects the inferred water-layer thickness. A comparison across elastic-media models and alternative elastic parameters, along with thickness probability density distributions, are therefore warranted. In the following, we use a Bayesian inversion framework to test how alternative rock-physics models affect the inference of liquid water in Mars' mid-crust.

2. Methods

Multiple studies suggest a predominantly basaltic Martian crust (McSween et al., 2009; Adam et al., 2009; McSween Jr, 2015), motivating specific choices of elastic rock-physics theories and parameters. We adopt the Bayesian scheme of Wright et al. (2024) (Tarantola, 2005) to expand the study space using a consistent methodology. In addition to SCM with Voigt mixing (Voigt, 1910; Hill, 1952), we test seven alternative configurations: SCM with Hill mixing (Hill, 1952); KT (Kuster and Toksoz, 1974); VRH (Hill, 1952); DEM (Berryman et al., 2002) with Voigt and with Hill mixing (Voigt, 1910; Reuss, 1929; Hill, 1952); and HS bounds (Mavko et al., 2020; Avseth et al., 2020) with Voigt and with Hill mixing (Table 1).

We test three primary sets of elastic parameters for the Martian crust, derived from recent analyses of InSight seismic data (Table 2). These sets represent a range of findings based on different event selections and inversion methods: (1) $V_p = 3.8$ km/s, $V_s = 2.2$ km/s, computed from a single, distant marsquake event (Li et al., 2022). (2) $V_p = 4.1$ km/s, $V_s = 2.5$ km/s representing the parameters used by Wright et al. (2024), which are averages of the results from multiple studies (Knapmeyer-Endrun et al., 2021; Duran et al., 2022; Carrasco et al., 2023; Joshi et al., 2023; Wieczorek et al., 2022; Lewis et al., 2019; Johnson et al., 2021). (3)$V_p = 4.7$ km/s, $V_s = 2.7$ km/s is obtained using a geodynamically constrained inversion of differential arrival times from 17 marsquake events (Drilleau et al., 2022). In the inversion process, all three elastic parameter configurations use the same bulk density, $\rho_b = 2589 \pm 157$ kg/m^3.

This combination of 8 theory configurations and 3 seismic parameter sets yields 24 model-data combinations for our analysis. With these combinations, we span a wider range of possible rock-physical combinations for the Martian mid-crust, which also incorporate the model of Wright et al. (2024) as a reference. One goal is to test the robustness of the inferred posteriors against the specific rock-physics and parameter assumptions underlying the Bayesian inversion (Tarantola, 2005). The sampling algorithm and convergence are detailed in Section 2.1 and Supplementary Section S2.

We use a common prior bulk-density as shown in the last column of Table 2 in all inversions as no other density estimates are available in the literature.

Table 3
Model parameter bounds used in the Bayesian inversion.

Parameter	Symbol	Range
water saturation	S_w	[0, 1]
porosity	ϕ	[0, 0.5]
crack aspect ratio	α	[0.001, 1]
mineral bulk modulus	κ_m	[75.6, 80] GPa
mineral shear modulus	μ_m	[25.6, 40] GPa
mineral density	ρ_m	[2680, 2900] kg/m^3

2.1. Inversion

Wright et al. (2024) use Bayesian inversion (Tarantola, 2005) to link the input elastic parameters with derived rock-physical parameters characterizing water presence in Mars Mid-crust. In this probabilistic framework, prior information is combined probabilistically with theoretical information to derive a posterior state of information:

$$\varsigma(\mathbf{m},\mathbf{d}) \propto \Theta(\mathbf{m},\mathbf{d})\,\varrho(\mathbf{m},\mathbf{d}), \tag{1}$$

where $\varrho(\mathbf{m},\mathbf{d})$ is the prior joint probability density function (PDF) defined over the data (3-dimensional) and model (6-dimensional) manifolds, while $\Theta(\mathbf{m},\mathbf{d})$ and $\varsigma(\mathbf{m},\mathbf{d})$ are theoretical and posterior PDFs defined on the same space. The data space is the collection of admissible elastic parameters, $\mathbf{d} = (V_p, V_s, \rho_b)$. Individually, the data variables are assumed independent and normally distributed with means and standard deviations given in Table 2. The model vector $\mathbf{m} = (S_w, \phi, \alpha, \kappa_m, \mu_m, \rho_m)$ is assigned independent uniform priors across each variable (Table 3) (Kilburn et al., 2022) (parameter α is not used by the VRH and HS theories; for KT and DEM, α is explored logarithmically, with $\alpha = 10^{\hat{\alpha}}$, $\hat{\alpha} \in [-3, 0]$.) Forward rock-physical simulation described by the theoretical joint PDF $\Theta(\mathbf{d},\mathbf{m})$ encodes the theory linking model to data (Table 1). The posterior joint PDF $\varsigma(\mathbf{m},\mathbf{d})$ is proportional to the product of the theoretical and prior joint PDFs, encapsulating both prior information about model and data parameters and their uncertainties, as well as the theoretical relations between them and associated uncertainty due to parameter selections. Marginal PDFs such as $\varsigma_\phi(\phi)$ are obtained by integrating the posterior joint PDF over all other variables.

After obtaining the posterior marginal PDFs $\varsigma_\phi(\phi)$ and $\varsigma_{S_w}(S_w)$, the equivalent water-layer thickness D_{water} can be evaluated by

$$D_{\text{water}} = D_{\text{mid-crust}}\,\phi\,S_w, \tag{2}$$

with the thickness of Mars' mid-crust $D_{\text{mid-crust}} \approx 8.5$ km (11.5–20 km depth) (Wright et al., 2024). Rather than substituting single summary statistics into the equation, we evaluate D_{water} for every accepted sample $(\phi_i, S_{w,i})$ in the Monte Carlo ensemble, thereby propagating the full uncertainty in both porosity and water saturation into a posterior distribution of thickness. This differs from the approach of Wright et al. (2024), who computed a single thickness estimate using the modes (highest peaks) of the posterior distributions ς_ϕ and ς_{S_w} independently. This approach is also implemented in Supplementary Section S1 for the purpose of comparison and verification.

Direct PDF operations in high dimensions are computationally expensive, so we use a Markov chain Monte Carlo (MCMC) approximation, as also employed by Wright et al. (2024). Specifically, we adopt the affine-invariant ensemble sampler of Goodman and Weare (2010) as implemented in `emcee` (Foreman-Mackey et al., 2013), the same affine-invariant ensemble sampler (the stretch move with $a = 2$) used by Wright et al. (2024). The two procedures are not identical in every detail—we initialize the walkers from the uniform priors (a cold start; see below) rather than reproducing the 500-step, RMSE-filtered warm start of Wright et al. (2024)—but Supplementary Section S2 shows this initialization choice shifts the posteriors negligibly (the median water-layer thickness changes by ≤ 0.11 km across all 24 cases), so that any material difference from their result reflects the rock-physics model and elastic-parameter choices we vary rather than the sampling procedure. The sampler maintains an ensemble of $N_w = 3\,n_{\text{dim}}$ walkers ($N_w = 18$ for the six-parameter theories and $N_w = 15$ for VRH, which omits α) that explore the posterior in parallel. To preserve detailed balance under simultaneous walker updates, the ensemble is partitioned into two sub-ensembles of approximately equal size that are updated alternately: walkers in the currently updating sub-ensemble propose moves using partners drawn uniformly at random from the other (frozen) sub-ensemble. Within each half-step the $N_w/2$ proposals are statistically independent and may be evaluated in parallel.

At each step, walker X_k proposes a new state $\mathbf{Y}$ by reaching toward its partner X_j,

$$\mathbf{Y} = X_j + z\,(X_k - X_j), \tag{3}$$

where z is a scalar drawn from $g(z) \propto 1/\sqrt{z}$ on $[1/a, a]$ with $a = 2$. The proposal is evaluated through the likelihood

$$L(\mathbf{m}) = \varrho_d\big(\Theta(\mathbf{d} \mid \mathbf{m})\big), \tag{4}$$

where $\Theta(\mathbf{d} \mid \mathbf{m})$ is the (possibly deterministic) forward prediction from $\mathbf{m}$ and ϱ_d is the prior marginal PDF over the data variables, and accepted with probability

$$A(X_k \to \mathbf{Y}) = \min\left(1,\; z^{n_{\text{dim}}-1}\,\frac{L(\mathbf{Y})}{L(X_k)}\right), \tag{5}$$

where n_{dim} is the dimension of the parameter space. The factor $z^{n_{\text{dim}}-1}$ is the Jacobian of the stretch move and ensures detailed balance with respect to the target posterior; its derivation is given in Goodman and Weare (2010). The affine invariance of this sampler removes the need to hand-tune a proposal covariance to match the strongly differing scales of ϕ, S_w, α, and the mineral moduli. All walkers are initialized by independent draws from the uniform model priors (a "cold start"), and we run the sampler for 50,000 steps per walker, discarding the first 1,000 as burn-in. Convergence diagnostics for all 24 inversions—including a check that the posteriors are insensitive to this initialization, obtained by re-running every case from the warm-start resampling protocol of Wright et al. (2024)—are reported in Supplementary Section S2.

2.2. Rock-physical theories

The following describes the rock-physical theories used, as well as their assumptions and limitations.

Continuous (partially saturated) treatment.. SCM, DEM, and HS require a model for the bulk modulus of the pore fluid, as they do not, by themselves, mix multiple fluid types. We implement two different **fluid mixing** models, Voigt and Hill (Voigt, 1910; Hill, 1952), to test a key assumption: how the fluids are physically distributed in the pore space. The Voigt average represents a stiff, segregated fluid scenario, while the Hill average provides a compromise between the stiff Voigt bound and the soft Reuss (or Wood's) mixing (Reuss, 1929; Wood, 1955; Hill, 1952). In our primary, continuous treatment, water saturation is drawn from a uniform prior over the full interval $S_w \in [0, 1]$ (first row of Table 3). Wherever the pore space is then partially saturated ($0 < S_w < 1$), gas and liquid both occupy the pores and a fluid-mixing law is required; testing the Voigt and Hill pair brackets this unknown fluid distribution and quantifies how much the mixing choice impacts the final water-volume estimates.

The Voigt mixing of bulk modulus κ_{fv} is defined as (Voigt, 1910; Hill, 1952):

$$\kappa_{fv} = S_w\,\kappa_{f1} + (1 - S_w)\,\kappa_{f2}. \tag{6}$$

Here f_1 denotes water, f_2 gas, and f_v the mixture. We use $\kappa_{f1} = 2.2$ GPa and $\kappa_{f2} = 0$ GPa, identical to Wright et al. (2024). Physically, Voigt mixing implies patchy saturation and corresponds to the stiff mixing end member. The Reuss average (Wood's formula), κ_{fr}, represents perfect fluid mixing and yields the soft end member (Reuss, 1929; Wood, 1955; Mavko et al., 2020):

$$\kappa_{fr} = \left(\frac{S_w}{\kappa_{f1}} + \frac{1 - S_w}{\kappa_{f2}}\right)^{-1}. \tag{7}$$

In the Martian environment, both end members are unlikely to hold everywhere, so Hill's average—the arithmetic mean of Voigt and Reuss—provides a reasonable compromise (Voigt, 1910; Reuss, 1929; Hill, 1952):

$$\kappa_f = \frac{\kappa_{fr} + \kappa_{fv}}{2}. \tag{8}$$

For the Hill average, we set $\kappa_{f2} = 0.015\,\text{GPa}$ to avoid the singularity in the Reuss bound when $\kappa_{f2} = 0$. This value is small relative to $\kappa_{f1} = 2.2\,\text{GPa}$, and the Hill average is insensitive to the precise choice: varying κ_{f2} over an order of magnitude produces negligible changes in the inversion results.

Binary (saturated/dry) end-member analysis. The partially saturated zone is limited in vertical extent on Earth, and the physically cleanest description at mid-crustal depth is arguably not a continuum at all: at these pressures the pore space is most naturally either fully dry or fully saturated. Following (Wright et al., 2025) (in their Reply to the Comment of Xiao et al. (2025)), we therefore also recast saturation as a binary choice between these two end-members, restricting S_w to the two values $\{0, 1\}$ rather than the continuous interval $[0, 1]$ of Table 3. This changes only the saturation row of Table 3; the priors on all other parameters (ϕ, α, κ_m, μ_m, ρ_m) are left unchanged, isolating the effect of the saturation assumption, and because each end-member fills the pore space with a single phase, no fluid-mixing law is needed and the Voigt–Hill ambiguity disappears entirely. The binary view removes the prior dependence inherent in choosing a continuous distribution for S_w and reduces the inversion to a Bayesian model-selection problem between two well-defined hypotheses, which we apply to all eight rock-physics theories and three velocity cases.

For each theory and velocity case, we run two separate inversions: a *wet* run with $S_w \equiv 1$ and a *dry* run with $S_w \equiv 0$. All other parameters retain the prior ranges of Table 3, and the MCMC procedure is otherwise as in the continuous inversion (Section 2.1). For each end-member we compute the Bayesian evidence

$$Z_{\text{wet/dry}} = \int p(\mathbf{d} \mid \mathbf{m}, S_w{=}1/0)\, p(\mathbf{m})\, \mathrm{d}\mathbf{m} \tag{9}$$

by prior Monte Carlo integration with N_e samples drawn from the joint prior over the remaining parameters. We use $N_e = 10^5$ for every theory except the two Differential Effective Medium configurations (Theories 5 and 6), whose more costly forward model (numerical integration of the DEM equations) limits us to $N_e = 2 \times 10^4$. The wet-fraction probability is then

$$P_{\text{wet}} = \frac{Z_{\text{wet}}}{Z_{\text{wet}} + Z_{\text{dry}}}, \tag{10}$$

and the binary thickness posterior is the corresponding mixture: with probability P_{wet} the thickness is drawn from $D_{\text{mid-crust}} \cdot \phi$ under the wet posterior, and with probability $1 - P_{\text{wet}}$ it is identically zero. The resulting wet/dry probabilities and binary thickness statistics are reported in Section 3.3.

Gassmann–Biot relation. The SCM and HS theories operate on the dry frame and do not directly incorporate fluid fill. We use the Gassmann–Biot equation (Gassmann, 1951; Biot, 1956; Mavko et al., 2020), i.e., fluid substitution, to obtain the effective bulk modulus κ_e from the dry-frame modulus κ_d (Wright et al., 2024; Mavko et al., 2020) using:

$$\kappa_e = \kappa_d + \frac{\left(1 - \dfrac{\kappa_d}{\kappa_m}\right)^2}{\dfrac{\phi}{\kappa_f} + \dfrac{1-\phi}{\kappa_m} - \dfrac{\kappa_d}{\kappa_m^2}}. \tag{11}$$

Here, ϕ is the porosity, κ_e is the effective bulk modulus of the final fluid-saturated rock, κ_d and κ_m are the bulk moduli of the dry rock frame and solid mineral matrix, and κ_f is the effective bulk modulus of the pore fluid mixture as calculated by the Voigt or Hill models. The resulting P-wave (V_p) and S-wave (V_s) velocities are calculated using the rock's total bulk density, ρ_b, and its effective shear modulus, as

$$V_p = \left(\frac{\kappa_e + \frac{4}{3}\mu_e}{\rho_b}\right)^{1/2}, \qquad V_s = \left(\frac{\mu_e}{\rho_b}\right)^{1/2}, \tag{12}$$

with $\mu_e = \mu_d$ in the seismic (low-frequency) limit.

Bulk density.. To obtain ρ_b in the data vector, we use a volume-weighted average over the constituent densities:

$$\rho_b = (1-\phi)\,\rho_m + \phi\left(S_w\,\rho_{f1} + (1 - S_w)\,\rho_{f2}\right), \tag{13}$$

where $\rho_{f1} = 1000\ \text{kg/m}^3$(water) and $\rho_{f2} = 0.02\ \text{kg/m}^3$(gas). This volumetric average is a direct application of the definition of bulk density ($\rho_b = m_{\text{total}}/V_{\text{total}}$), where the total mass is the sum of the masses of the rock matrix, water, and gas components.

2.2.1. Dry-frame theories

We test five different dry-frame theories—SCM, HS, DEM, KT, and VRH—to model the rock's solid skeleton. Each of these theories makes different physical assumptions about pore geometry and mineral mixing, and the following subsections detail how each is implemented.

Berryman's SCM (Wright et al., 2024; Berryman, 1980). In dry-frame rock physics, several factors impact the bulk and shear moduli, including κ_m/μ_m ratio, as well as porosity ϕ, water saturation S_w, and aspect ratio α. The solid phase carries all shear and most bulk resistance, and its fraction controls stiffness. The aspect ratio α governs stress concentration around pores. Berryman's SCM (Berryman, 1980) incorporates these factors to obtain κ_d and μ_d via

$$\begin{aligned} (1-\phi)\left(\kappa_m - \kappa_d\right) P \;+\; \phi\left(\kappa_f - \kappa_d\right) P \;&=\; 0, \\ (1-\phi)\left(\mu_m - \mu_d\right) Q \;+\; \phi\left(\mu_f - \mu_d\right) Q \;&=\; 0, \end{aligned} \tag{14}$$

where P and Q are shape factors solved iteratively from α. Despite its generality, the scheme may fail to converge at specific α when $\mu_f = 0$.

Hashin–Shtrikman (Hashin and Shtrikman, 1963). The HS method provides tight bounds on dry-frame moduli. It accounts for the κ_m/μ_m ratio and porosity ϕ. Here we adopt the modified HS and include critical porosity ϕ_c (the threshold above which the system behaves fluid-like) (Avseth et al., 2020; Gal et al., 1998). The theory is relatively insensitive to the pore aspect ratio and places more emphasis on the ratio ϕ/ϕ_c. The Hashin-Shtrikman lower bound (LB) represents the softest possible effective moduli for an isotropic composite. It is derived from a physical model where the softest material (the pore space) forms the core of a composite sphere and the stiffest material (the mineral matrix) forms the outer shell. This configuration is the most compliant (softest), and its bulk and shear moduli, $\kappa_{\text{d}}^{\text{LB}}$ and $\mu_{\text{d}}^{\text{LB}}$ are given by:

$$\begin{aligned} \kappa_{\text{d}}^{\text{LB}}(\phi) &= \left[\frac{\frac{\phi}{\phi_c}}{\kappa_c + \frac{4}{3}\mu_c} + \frac{1 - \frac{\phi}{\phi_c}}{\kappa_m + \frac{4}{3}\mu_c}\right]^{-1} - \frac{4}{3}\mu_c, \\ \mu_{\text{d}}^{\text{LB}}(\phi) &= \left[\frac{\frac{\phi}{\phi_c}}{\mu_c + \zeta_c} + \frac{1 - \frac{\phi}{\phi_c}}{\mu_m + \zeta_c}\right]^{-1} - \zeta_c, \\ \zeta_c &= \mu_c\,\frac{9\kappa_c + 8\mu_c}{6(\kappa_c + 2\mu_c)}. \end{aligned} \tag{15}$$

Here, ϕ_c is the critical porosity, which we set to 0.7, typical of high-velocity lava facies (Avseth et al., 2020). The terms κ_c and μ_c are the frame moduli at this critical porosity. They are often set to small values because the pressure that holds the grains together at critical porosity is minimal (Avseth et al., 2020). We set both variables to 1 GPa for numerical stability. The ζ_c and ζ_m terms are intermediate shear moduli dependent on the frame and mineral moduli, respectively. The ϕ/ϕ_c and $1 - \phi/\phi_c$ weights apply to the pore and the solid fractions, respectively.

Table 4
Inclusion shape–dependent expressions for P^{mi} and Q^{mi} with aspect ratio cutoffs.

Inclusion shape (Aspect ratio $\hat{\alpha}$)	P^{mi}	Q^{mi}
Spheres $\hat{\alpha} \in (-2, 0]$	$\frac{\kappa_m + \frac{4}{3}\mu_m}{\kappa_i + \frac{4}{3}\mu_m}$	$\frac{\mu_m + \zeta_m}{\mu_i + \zeta_m}$
Penny cracks $\hat{\alpha} \in [-3, -2]$	$\frac{\kappa_m + \frac{4}{3}\mu_i}{\kappa_i + \frac{4}{3}\mu_i + \pi\alpha\beta_m}$	$\frac{1}{5}\left[1 + \frac{8\mu_m}{4\mu_i + \pi\alpha(\mu_m + 2\beta_m)} + 2\frac{\kappa_i + \frac{2}{3}(\mu_i + \mu_m)}{\kappa_i + \frac{4}{3}\mu_i + \pi\alpha\beta_m}\right]$

Notes: $\beta_x = \mu_x \frac{3\kappa_x + \mu_x}{3\kappa_x + 4\mu_x}$, $\zeta_x = \mu_x \frac{9\kappa_x + 8\mu_x}{6(\kappa_x + 2\mu_x)}$;
subscripts $x \in \{m, i\}$ denote matrix or inclusion.

The upper bound (UB) estimates the stiffest admissible dry moduli:

$$\kappa_d^{\mathrm{UB}}(\phi) = \left[\frac{1 - \frac{\phi}{\phi_c}}{\kappa_m + \frac{4}{3}\mu_m} + \frac{\frac{\phi}{\phi_c}}{\kappa_c + \frac{4}{3}\mu_m}\right]^{-1} - \frac{4}{3}\mu_m,$$
$$\mu_d^{\mathrm{UB}}(\phi) = \left[\frac{1 - \frac{\phi}{\phi_c}}{\mu_m + \zeta_m} + \frac{\frac{\phi}{\phi_c}}{\mu_c + \zeta_m}\right]^{-1} - \zeta_m, \tag{16}$$
$$\zeta_m = \mu_m \frac{9\kappa_m + 8\mu_m}{6(\kappa_m + 2\mu_m)}.$$

The true effective moduli of an isotropic rock must lie between these two bounds. As the exact pore geometry is unknown, we use the average of the bounds as a practical estimate of the homogeneous rock properties, which has been shown to be an accurate approximation (Mavko et al., 2020):

$$\kappa_d = \tfrac{1}{2}\left(\kappa_d^{\mathrm{UB}} + \kappa_d^{\mathrm{LB}}\right),$$
$$\mu_d = \tfrac{1}{2}\left(\mu_d^{\mathrm{UB}} + \mu_d^{\mathrm{LB}}\right). \tag{17}$$

These average bounds hold for arbitrary inclusion geometry, which implies random distribution of cracks with various shapes. The averaged moduli are thus broadly applicable.

Differential Effective Medium (Berryman et al., 2002). Like Berryman's SCM (Berryman, 1980; Wright et al., 2024), DEM accounts for the κ_m/μ_m ratio, as well as ϕ, S_w, and α. Instead of solving for the effective moduli in one step, DEM adds inclusions incrementally until the target ϕ is reached:

$$(1 - \phi)\frac{d\kappa_e}{d\phi} = \left(\kappa_f - \kappa_e\right) P^{mi},$$
$$(1 - \phi)\frac{d\mu_e}{d\phi} = \left(\mu_f - \mu_e\right) Q^{mi}. \tag{18}$$

Here $\kappa_e(\phi)$ and $\mu_e(\phi)$ start at mineral moduli; P^{*i}, Q^{*i} are shape factors (Table 4) (Mavko et al., 2020). We solve the DEM differential equations using a numerical integration scheme based on the method described by Berryman (1992). We use a small integration step size of $\Delta\phi = 10^{-3}$ to ensure numerical stability and convergence of the solution. To avoid non-convergence when $\kappa_i = 0$, we use the piecewise definitions in Table 4, which treat inclusions as penny-shaped cracks ($\alpha \le 10^{-2}$) or spheres ($\alpha > 10^{-2}$). The aspect ratio α is a prior variable in the inversion, explored log-uniformly by sampling its exponent, $\hat{\alpha}$, from a standard uniform distribution over the range $[-3, 0]$, where $\alpha = 10^{\hat{\alpha}}$. The $\hat{\alpha}$ range, corresponding to $\alpha \in [0.001, 1]$, covers the full spectrum of expected pore shapes from flat microcracks to spherical vesicles. This incremental approach, combined with the piecewise shape factors, captures the progressive, non-linear softening of the rock with increasing porosity.

Kuster–Toksöz (Kuster and Toksoz, 1974). KT computes effective moduli without invoking a fluid-mixing law or fluid substitution (Kuster and Toksoz, 1974). It considers κ_m/μ_m, ϕ, S_w, α, and the moduli of each fluid phase:

$$(\kappa_e - \kappa_m)\frac{\kappa_m + \frac{4}{3}\mu_m}{\kappa_e + \frac{4}{3}\mu_m} = \phi[\, S_w(\kappa_{f1} - \kappa_m) P^{mi} + (1 - S_w)(\kappa_{f2} - \kappa_m) P^{mi}],$$
$$(\mu_e - \mu_m)\frac{\mu_m + \zeta_m}{\mu_e + \zeta_m} = \phi[\, S_w(\mu_{f1} - \mu_m) Q^{mi} + (1 - S_w)(\mu_{f2} - \mu_m) Q^{mi}]. \tag{19}$$

Like DEM, KT uses shape factors, and we explore α log-uniformly. Its key significance in the Martian context is how it models patchy saturation. Unlike the SCM and HS models, which use the Voigt average to create a single effective fluid that is then substituted into a dry frame, KT's formulation treats water-filled cracks and gas-filled cracks as two separate inclusion families and computes their combined effect simultaneously. This makes it an important reference point for all other models in this study that assume patchy saturation (i.e., those using Voigt mixing). It allows us to test if the method of implementing patchy saturation (premixing the fluid vs. treating inclusions separately) significantly alters the inversion results. The approach is efficient at low inclusion concentrations, although it does not explicitly model interactions among inclusions.

Voigt–Reuss–Hill (Voigt, 1910; Reuss, 1929; Hill, 1952). In contrast to the previous models that depend on pore geometry, the Voigt-Reuss-Hill (VRH) average is a simple mixing law that accounts only for the volume fractions of the mineral and fluid constituents (Voigt, 1910; Reuss, 1929; Hill, 1952). It entirely disregards the influence of pore shape (i.e., the aspect ratio α). The framework resembles mixing laws but includes the solid phase explicitly, so no fluid substitution is required.

The Voigt average represents the stiffest possible theoretical bound, corresponding to the isostrain condition (Mavko et al., 2020). This model assumes all components (mineral, water, and gas) are forced to deform by the same amount, which maximizes the internal stress. This makes the composite material highly non-compliant and yields the largest possible elastic moduli:

$$\kappa_V = (1 - \phi)\kappa_m + \phi S_w \kappa_{f1} + \phi(1 - S_w)\kappa_{f2},$$
$$\mu_V = (1 - \phi)\mu_m + \phi S_w \mu_{f1} + \phi(1 - S_w)\mu_{f2}. \tag{20}$$

Conversely, the Reuss average represents the most compliant theoretical bound, corresponding to the isostress condition. This model assumes all components experience the same stress, which is the softest possible arrangement (e.g., layered perpendicular to the stress):

$$\kappa_f = S_w \kappa_{f1} + (1 - S_w)\kappa_{f2},$$
$$\frac{1}{\kappa_R} = \frac{1 - \phi}{\kappa_m} + \frac{\phi}{\kappa_f}, \tag{21}$$
$$\mu_R = 0.$$

Hill's mean provides the effective moduli:

$$\kappa_e = \tfrac{1}{2}(\kappa_V + \kappa_R),$$
$$\mu_e = \tfrac{1}{2}(\mu_V + \mu_R). \tag{22}$$

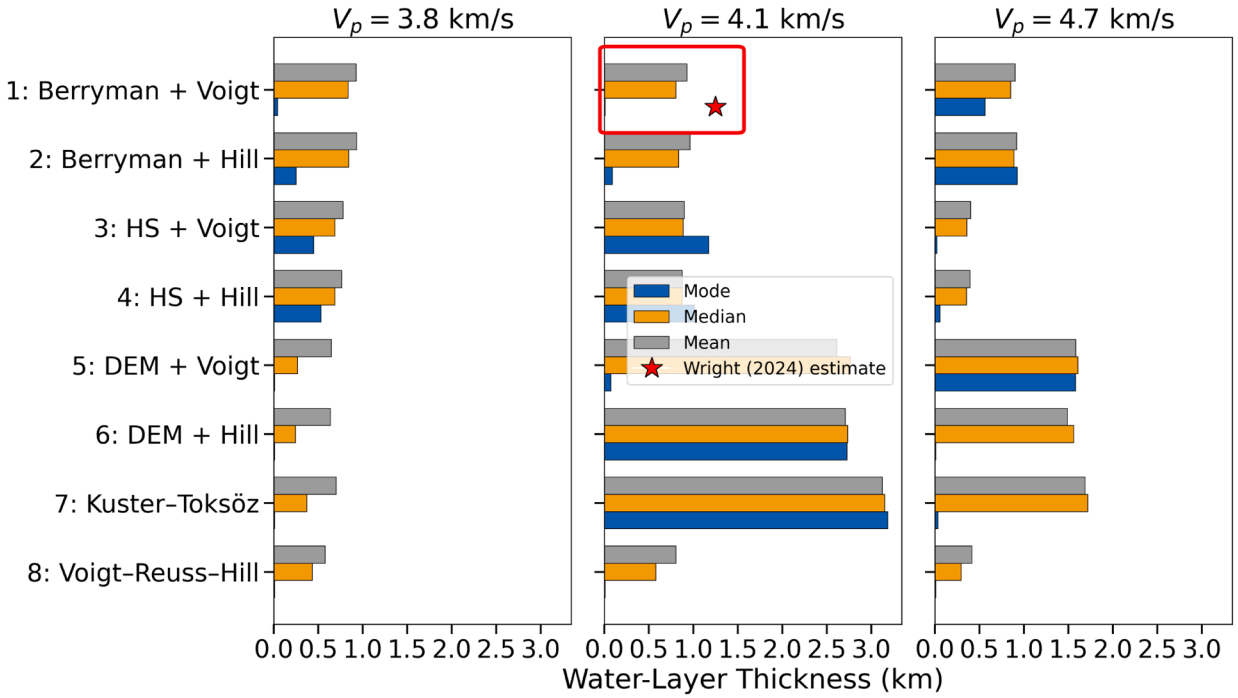


Fig. 1. Summary statistics (mode, median, and mean) of the posterior water-layer thickness distribution for all eight theories across three velocity cases. The red star marks the mode-based estimate of Wright et al. (2024), computed by substituting the marginal modes of porosity and water saturation into the thickness equation. The red box highlights Theory 1 at V_p = 4.1 km/s, corresponding to the rock-physics framework and velocity case used by Wright et al. (2024).

Unlike SCM, KT, and DEM, VRH omits α, implicitly allowing nonuniform crack shapes and densities. Although primarily an estimate, VRH V_p has been shown to be reasonable in analogous terrestrial middle crust (Kitamura and Ishikawa, 1998).

3. Results and discussion

Using the inversion scheme developed in the Methods section, we ran 50,000 MCMC iterations for each model–parameter set, as shown in Tables 1, 2, and Fig. 1 (convergence of all Markov chains was confirmed using standard diagnostics; details are provided in Supplementary Section S2). The Wright et al. (2024)-style inversion is also conducted for reference (see Supplementary Section S1).

3.1. Posterior water-layer thickness across models and seismic inputs

Figs. 1 and 2 together summarize the posterior water-layer thickness for all eight theories across the three velocity cases: Fig. 1 reports the mode, median, and mean of each posterior, while Fig. 2 shows the full distributions behind those summaries. Throughout, we use *mode* for the location of a PDF's global maximum—its single most probable value—and reserve *peak* for any local maximum, so that a multimodal posterior may have several peaks but only one mode (its tallest peak); we distinguish both from the median and mean. A striking feature is that the mode of a majority of distributions lies near zero, indicating that a dry or nearly dry mid-crust is the most probable outcome under most rock-physics frameworks. The notable exceptions are Theories 5, 6, and 7 (DEM and Kuster–Toksöz) at V_p = 4.1 and 4.7 km/s, where the distributions shift to substantially higher thicknesses (median thickness of approximately 3 km at V_p = 4.1 km/s and 1.7 km at V_p = 4.7 km/s), and Theories 1 and 2 (Berryman SCM + Voigt/Hill) at V_p = 4.7 km/s, where broad distributions with modes away from zero emerge. For Theories 3 and 4 (Hashin–Shtrikman), the two lower-velocity cases (V_p = 3.8 and 4.1 km/s) yield broad distributions with possibilities of wet crust, while the V_p = 4.7 km/s case points to the lowest water content of the three.

A notable feature of Fig. 1 is that the inferred water does not vary monotonically with V_p: for several theories (notably HS, DEM, and KT) the thickness mode is largest at the intermediate V_p = 4.1 km/s case rather than at the lowest or highest V_p. The reason is that the relevant fluid indicator is the ratio V_p/V_s, not V_p alone, and V_p/V_s is itself nonmonotonic across the three InSight-derived cases (1.73, 1.64, and 1.74 at V_p = 3.8, 4.1, and 4.7 km/s; Table 5): the intermediate case carries the *lowest* V_p/V_s and therefore, in general, admits the largest $\phi \cdot S_w$—and hence produces the largest amount of water.

Because the HS bounds describe the dry-frame response from volume fractions alone, without a microgeometric (aspect-ratio) parameter, the seismic data map almost directly onto porosity, saturation, and the mineral moduli. Since fluid contributes nothing to shear ($\mu_e = \mu_d$), V_s and μ_m together fix the porosity through the HS shear bound, with the largest admissible porosity reached at the prior maximum μ_m = 40 GPa. The V_p = 4.7 km/s case carries the highest V_p/V_s ratio and therefore the largest demanded bulk modulus, $\kappa_e = \rho_b\left(V_p^2 - \frac{4}{3}V_s^2\right) \approx 32$ GPa. Even at the maximum porosity that its V_s permits ($\phi \approx 0.12$), the narrow prior on κ_m (75.6–80 GPa) pins the HS dry-frame modulus at $\kappa_d \approx 31$ GPa, already accounting for nearly all of κ_e; the Gassmann–Biot substitution (Eq. (11)) then need only supply ≈ 1 GPa, corresponding to a low saturation ($S_w \approx 0.13$ for Voigt and ≈ 0.25 for Hill mixing). The V_p = 4.7 km/s data thus favor both low porosity and low saturation, and because water-layer thickness scales with the product $\phi\, S_w$ (Eq. (2)), the inferred water layer is thin. The lower-velocity cases carry a smaller κ_e and therefore admit higher porosity; through the bulk-density balance (Eq. (13)), reproducing the observed ρ_b across that larger pore volume requires the pores to be water-filled, shifting those posteriors toward the broad, wet distributions. This account is conditioned on the adopted prior box: the near-fixed κ_m and bounded ρ_m that govern the porosity and saturation here are properties of the basalt-consistent bounds of Table 3, not of the data alone, and Supplementary Section S3 shows—for the SCM + Voigt configuration—that widening them can move the inference between a dry and a wet mid-crust.

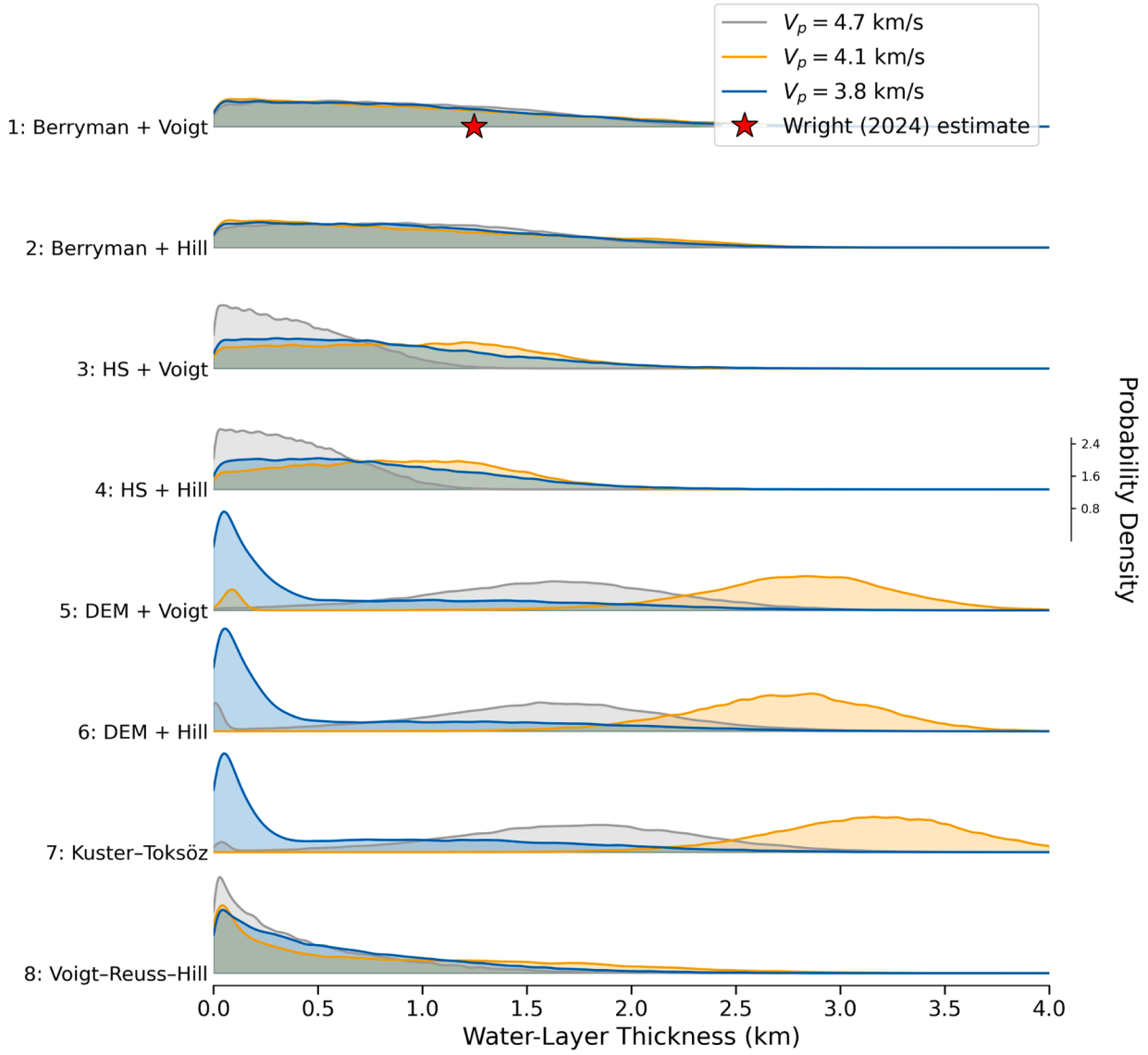


Fig. 2. Ridgeline plot of posterior water-layer thickness distributions for all eight rock-physics theories. Each row shows the three velocity cases overlaid. Most distributions have their mode near zero, indicating a dry or nearly dry mid-crust as the most probable outcome. Theories 5 to 7 demonstrate multimodal geometries, with the $V_p = 4.1$ and $V_p = 4.7$ km/s cases shifted to higher thickness values. All theories are drawn on a single common vertical (probability-density) scale, so peak heights are directly comparable across rows.

As seen in Fig. 1, nearly all distributions are strongly right-skewed. For a strictly positive quantity such as water-layer thickness the ordering mode ≤ median ≤ mean is expected in general, so the direction of the inequality is not in itself informative; what matters here is the *magnitude* and *location* of the separation, neither of which positivity guarantees. The mode sits near zero while the median and mean lie up to an order of magnitude higher, so the choice of summary statistic is decisive: a mode-based thickness and a mean- or median-based thickness can differ by a factor of ~10 for the same posterior. For instance, Theory 8 has modes near zero yet median thicknesses of 0.3–0.7 km, illustrating that the right tail, rather than the mode, drives the central-tendency statistics.

The anomalous behavior of Theories 5 to 7 arises from the piecewise-defined shape factors in the Kuster–Toksöz formulation, which introduce geometric discontinuities that can shift the inferred thickness to unrealistically high values (Eq. (19)). The similarity between the DEM and KT thickness distributions at these velocities reflects the shared dominance of the piecewise shape factors P^{mi} and Q^{mi} (Table 4), whose influence on the inferred thickness is more substantial than the choice of fluid mixing and dry frame theories.

Table 5
Across-theory disagreement in inferred water content for the three seismic datasets. The intermediate-V_p dataset has the lowest V_p/V_s ratio and the largest disagreement among the eight rock-physics theories, measured both as across-theory range of $\phi \cdot S_w$ (the range of per-theory median) and as its coefficient of variation (CoV, the standard deviation of the eight medians divided by their mean).

V_p (km/s)	3.8	4.1	4.7
V_p/V_s	1.73	1.64	1.74
Across-theory range of $\phi \cdot S_w$	0.070	0.302	0.167
CoV (%)	42	65	59

Table 5 quantifies this. Beyond driving the non-monotonic mode noted above, the low V_p/V_s of the intermediate $V_p = 4.1$ km/s case coincides with by far the largest *disagreement* among the eight rock-physics theories. The per-theory median $\phi \cdot S_w$ spans a range of 0.302 — more than four times that of the $V_p = 3.8$ km/s case (0.070) and roughly

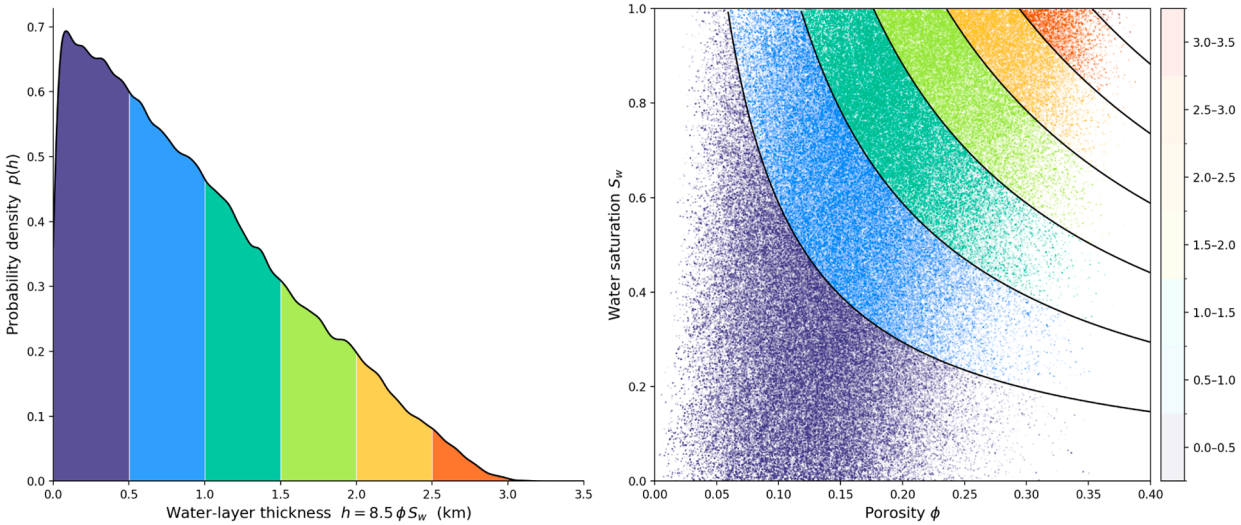


Fig. 3. Geometric origin of the water-layer-thickness distribution for the Berryman SCM at $V_p = 4.1$ km/s (Theory 1, the configuration of Wright et al. (2024)). **Left:** posterior of water-layer thickness $h = D_{\text{mid-crust}}\,\phi\,S_w$, partitioned into equal-width 0.5 km bands. **Right:** the same posterior samples in the (ϕ, S_w) plane, colored by the thickness band of each sample; black curves are the corresponding isothickness contours $\phi\,S_w = \text{const}$. The low-thickness bands carry the *most* probability (tallest slices, left) yet occupy a large area of the (ϕ, S_w) plane and appear sparse (right), while the high-thickness bands are confined to a small, dense corner. This area effect makes the crossplot's apparent point density a misleading guide to where the thickness probability lies.

twice that of the $V_p = 4.7$ km/s case (0.167). The coefficient of variation, which normalizes the dispersion of the eight medians by their mean and is therefore insensitive to the overall water level of each case, tells the same story: it rises from 42% at $V_p = 3.8$ km/s to 65% at $V_p = 4.1$ km/s before easing to 59% at $V_p = 4.7$ km/s. That both an absolute (range) and a scale-free (CoV) measure single out the intermediate-V_p case rules out the possibility that the apparent disagreement is an artifact of one outlier theory or of the higher mean water content itself. Because V_p/V_s is the standard fluid indicator, the intermediate-V_p observations fall in a region of parameter space where multiple model families admit a wider range of $\phi \cdot S_w$ combinations. The elevated water content at $V_p = 4.1$ km/s is then a direct consequence of this widened admissible range: when more theories admit higher $\phi \cdot S_w$, the right tail of the strongly right-skewed posteriors — which, as noted above, drives the median and mean — extends further. We therefore read this not as a physical mechanism unique to intermediate V_p, but as a sensitivity statement: how much water one infers depends strongly on which seismic dataset is used, and this dependence is sharpest precisely where V_p/V_s is most fluid-indicative.

The Berryman SCM results (Theories 1 and 2) deserve particular attention, as this is the rock physics employed by Wright et al. (2024). While the mode-based estimate of Wright et al. (2024) yields a thickness of ≈ 1.25 km for the $V_p = 4.1$ km/s case (Fig. 1), the full posterior distribution in fact has its mode near zero, indicating that a dry mid-crust is the single most probable outcome even under their own rock-physics model. The median and mean of the thickness distribution (≈ 0.8–0.9 km) are indeed non-negligible, but these summary statistics are inflated by the heavy right tail rather than reflecting a concentration of probability around ~ 1 km. This discrepancy has a simple geometric origin that is easily misread from the crossplot alone. Because the water-layer thickness is the product $D_{\text{water}} = D_{\text{mid-crust}}\,\phi\,S_w$ (Eq. (2)), a fixed thickness traces a hyperbola $\phi\,S_w = \text{const}$ in the (ϕ, S_w) plane, and equal thickness increments map to bands bounded by these hyperbolae (Fig. 3). These bands are strongly uneven in area: a low-thickness band sweeps a broad region of the (ϕ, S_w) plane, whereas a high-thickness band of the same width is confined to a thin sliver in the high-ϕ, high-S_w corner. A given amount of posterior probability is therefore spread thinly over a large area at low thickness but packed densely into a small area at high thickness. Read by eye, the crossplot's apparent point density thus understates the low-thickness region and draws attention to the high-ϕ/high-S_w corner—precisely where the marginal modes lie—even though that corner is a small-area band holding little of the total probability. When the joint posterior is instead integrated along each isothickness contour to form the thickness distribution (Fig. 3, left), the broad, sparse-looking low-thickness band dominates and the posterior peaks near zero, while the visually dense corner contributes little. The marginal-mode product $\phi'\,S_w'$ of Wright et al. (2024) reports the location of that dense corner rather than the mass of the distribution, and so overstates the thickness; equivalently, $\text{mode}(\phi \cdot S_w) \neq \text{mode}(\phi)\,\text{mode}(S_w)$.

3.2. The most parsimonious model–data combination

We describe the inferred water as *negligible* when the posterior places the majority of its probability below 0.5 km of equivalent water-layer thickness—roughly a quarter to a third of the Wright et al. (2024) estimate. By this distribution-based criterion, the most parsimonious combination of model and data—HS with Hill mixing at $V_p = 4.7$ km/s, for which 67% of the posterior thickness falls below 0.5 km (median 0.35 km)—points toward a negligible-water scenario, for two main reasons.

1. Data configuration: The three velocity configurations are not interchangeable measurements of a single quantity but the outputs of three different InSight analyses with different event selections, depth sensitivities, and inversion constraints (Table 2). Li et al. (2022) is based on a single distant marsquake, Wright et al. (2024) is an average over several earlier studies with heterogeneous methodologies, and Drilleau et al. (2022) is a geodynamically constrained inversion of differential arrival times from 17 marsquake events that resolves the full crustal velocity profile. Among the three, the Drilleau et al. (2022) configuration ($V_p = 4.7$, $V_s = 2.7$ km/s) rests on the largest event set and the most explicit physical constraints, and on those grounds carries the strongest methodological footing of the three. It is also the configuration most consistent with the rock-physical expectation that lithostatic pressure at mid-crustal depths closes compliant microcracks and drives the dry frame toward its intrinsic moduli (Sprunt and Nur, 1977); the lower-velocity estimates sit below that baseline and, within our rock-physics framework, can be reconciled only by introducing additional compliance — pore water is one such mechanism, but unclosed cracks, fine-scale layering, and elastic anisotropy are alternatives the present isotropic, fluid-substitution models do not span.

2. Model plausibility: The shape-factor models, 1–2 and 5–7, are limited by their high sensitivity to the crack aspect ratio (α). While the seismic data place a posterior constraint on α within each model, the inferred value of α — and the resulting water content — differs substantially between SCM, KT, and DEM, and no independent geological measurement of α is available for the Martian mid-crust to favor one model over another. Among the models that do not depend on aspect ratio (Theories 3–4 and 8), the HS model (Theories 3–4) provides physically grounded, strict bounds (Avseth et al., 2020), and its average moduli approximate the true elastic response better than VRH (Theory 8) alone. With this combination — HS with Hill mixing and the Drilleau et al. (2022) configuration (Theory 4) — the inversion most consistently returns a near-zero water-layer thickness. The mechanism is direct: the stiff elastic response implied by V_p = 4.7 km/s is compatible only with low-porosity configurations, and through the volumetric relation in Eq. (2), $D_{\text{water}} = D_{\text{mid-crust}}\,\phi\,S_w$, any low-$\phi$ posterior yields a small total water volume regardless of saturation. The low-water inference at this combination is therefore not a claim that the remaining pore space is dry — it is a claim that there is very little pore space to be filled. We present this combination not as the only admissible interpretation of the InSight data, but as the most parsimonious reading among the rock-physics theories we tested.

3.3. Binary (saturated/dry) end-member results

Applying the binary end-member inversion described in Section 2.2 to all eight rock-physics theories and three velocity cases yields the wet/dry probabilities and binary thickness statistics discussed here. Table 6 reports P_{wet} together with mode, median, and mean of the binary mixture thickness for each theory–velocity combination. The most parsimonious combination identified above—HS with Hill mixing (Theory 4) at V_p = 4.7 km/s—yields P_{wet} = 0.16, a median binary thickness of 0.00 km, and a 95th-percentile of 1.01 km. The binary framing therefore reinforces one central finding: even when saturation is forced to take only its end-member values, the data overwhelmingly favor the dry hypothesis under this combination. The original configuration of Wright et al. (2024)—SCM with Voigt mixing (Theory 1) at V_p = 4.1 km/s—yields P_{wet} = 0.74 and a binary thickness median of 1.54 km, faithfully reproducing their wet result. Across the HS theories, P_{wet} decreases monotonically with increasing V_p (from 0.58 at 3.8 km/s, to 0.40 at 4.1 km/s, to 0.16 at 4.7 km/s), mirroring the velocity-case sensitivity discussed above.

Crucially, *the wet/dry probability P_{wet} is not a measure of how much water is present.* It is a model-selection statistic—it reports how the data weight the two end-member hypotheses—but it conveys nothing about the thickness implied by the wet hypothesis. Fixing S_w = 1 assigns the entire pore volume to water, so the wet end-member predicts *more* water than the continuous-S_w inversion at the same porosity (for HS + Hill at V_p = 4.7 km/s the wet-branch median thickness is 0.89 km, versus 0.35 km for continuous S_w). At the same time, the dry end-member contributes a point mass at $D_{\text{water}} = 0$ whose density dominates the mixture whenever P_{dry} is appreciable: a mode-based reading of the binary mixture returns essentially zero (0.01–0.02 km) for *every* theory–velocity combination in Table 6, including those with $P_{\text{wet}} > 0.5$. Reporting $P_{\text{wet}} > P_{\text{dry}}$ alone is therefore not sufficient to establish a wet mid-crust.

Indeed, a high P_{wet} need not even imply a hydrologically significant layer, because the wet branch itself can be thin. At V_p = 3.8 km/s the DEM and Kuster–Toksöz theories (Theories 5–7) place ≈ 25–30% of their wet-branch probability below 0.5 km, and VRH (Theory 8) ≈ 10%, even though their wet fractions are 0.57–0.82: the low-porosity solutions these models admit yield little water despite S_w = 1 (Fig. 4). Both observations point to the same conclusion as the continuous analysis—the water content is characterized by the full thickness posterior, not by a wet/dry probability or any single summary statistic.

3.4. Effect of the fluid-mixing law

The effect of mixing-law choice on inferred water-layer thickness is model-specific and, in most cases, modest compared to the choice of rock-physics theory itself. As seen in Fig. 1, the SCM pair (Theories 1–2) shows virtually no visible difference between Voigt and Hill mixing across all three velocity cases in terms of mean and median, though Hill mixing yields a higher mode. For the HS pair (Theories 3–4), the two extreme velocity cases (V_p = 3.8 and 4.7 km/s) show slightly higher modes under Hill mixing. The DEM pair (Theories 5–6) exhibits the most notable mixing-law sensitivity: at V_p = 4.1 km/s, the Hill variant (Theory 6) produces a visibly higher mode than the Voigt variant (Theory 5), whereas at V_p = 4.7 km/s the Voigt variant shows a much higher mode. These differences reflect shifts in the relative heights of competing local maxima in the posterior thickness distributions, driven by the piecewise shape factors P^{mi} and Q^{mi} that govern how the forward model responds near the geometric transition boundary. Regardless, these mixing-law differences are an order of magnitude smaller than the spread across rock-physics theories (Fig. 1), confirming that the choice of mixing law is a secondary source of uncertainty.

3.5. Comparison with independent crustal analyses

Our conclusions can be placed in the context of the comprehensive rock-physics analysis of Knapmeyer-Endrun et al. (2025), whose four-layer crustal model beneath InSight assigns the 10–20 km interval (their layer 3) to essentially the same mid-crustal depths we consider here. Their preferred model for this interval is a dry, CO_2-filled basalt rather than a water-saturated rock (their Fig. 10), and they note independently that seismic attenuation requires a "heterogeneous and dry crust, excluding the presence of liquid water over a significant depth range like layer 2 or 3"—a constraint they point out was not considered by Wright et al. (2024) when modeling the mid-crust as water-saturated. These are independent lines of evidence, from a preferred lithological model and from wave attenuation rather than from rock-physics non-uniqueness, that converge on our own conclusion that abundant free liquid water at these depths is not robustly required by the data.

The same study also bears on the robustness of the prior mid-crustal estimate. Knapmeyer-Endrun et al. (2025) report that the pore aspect ratio favored by Wright et al. (2024) does not, in the independent modeling of Katayama and Akamatsu (2024), reproduce the velocity increase near 10 km depth, and that the two studies disagree about the appropriate aspect ratio; they further describe this aspect ratio as poorly constrained for the Martian crust. This supports both our concern that the inferred water content is sensitive to such weakly constrained geometric parameters and our emphasis on theory families, such as the Hashin–Shtrikman bounds, that require no aspect-ratio assumption. Consistent with this, in modeling the layer-3 velocities themselves Knapmeyer-Endrun et al. (2025) find that several lithologies (basalt, feldspar, and gabbro) and a range of porosity–aspect-ratio combinations fit the InSight constraints equally well (their Fig. 8), mirroring our central finding that the inferred mid-crustal water content is governed less by the data than by the choice of rock-physics model and elastic parameters. We stress that (Knapmeyer-Endrun et al., 2025) do infer liquid brine at shallower depths (their layer 1, ~200–2000 m) and pervasive but volumetrically minor hydrous alteration ($\lesssim$0.3 wt% water) throughout the crust; our agreement with them concerns specifically the absence of a robust requirement for a thick, free liquid-water layer in the mid-crust.

3.6. Caveats

All rock-physical formulations considered here assume homogeneity across seismic scale, which becomes unrealistic at depth where pressure and temperature increase (Mavko et al., 2020). The rock-physics models used here assume liquid water as the pore-filling

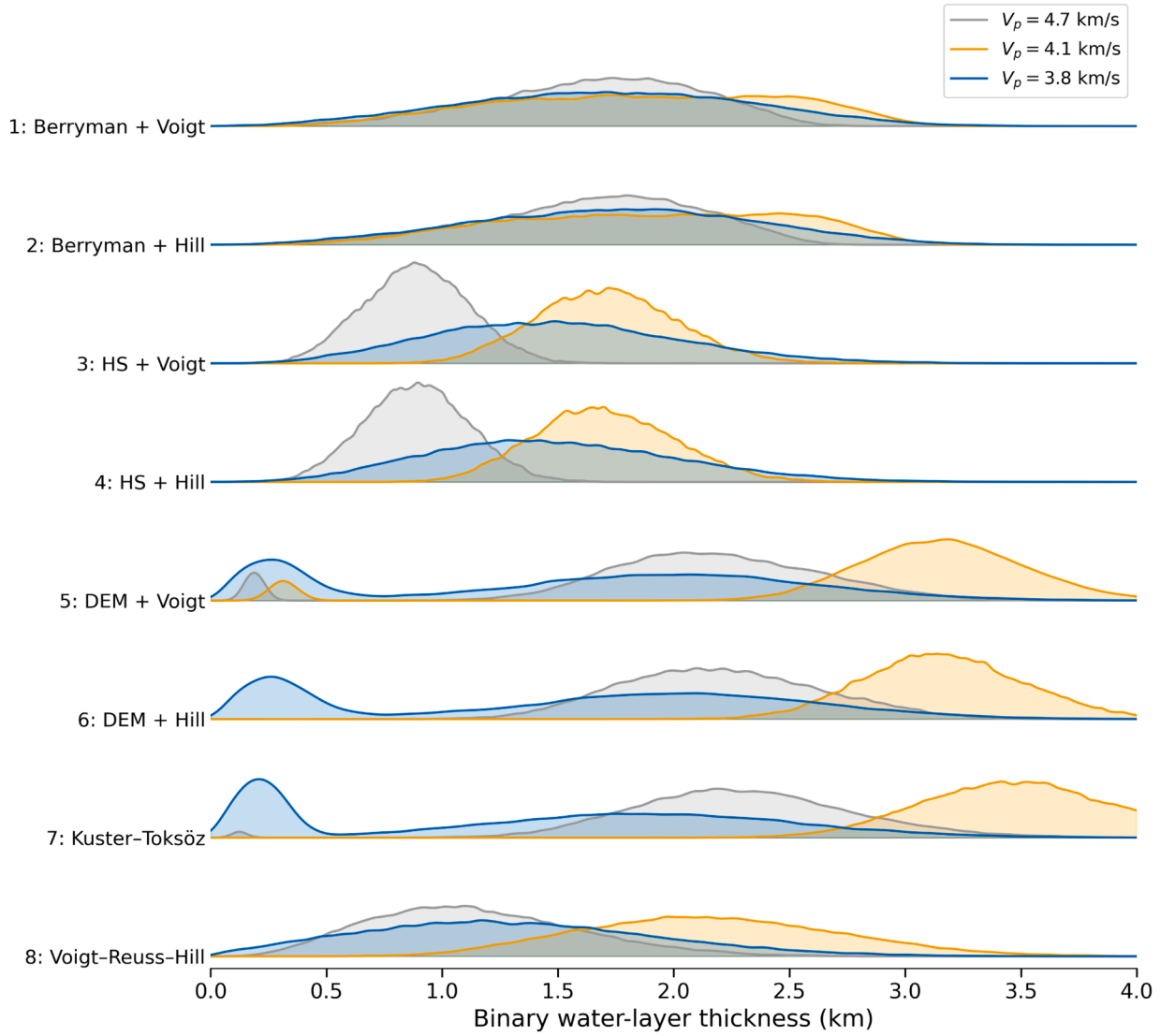


Fig. 4. Binary wet-branch thickness posteriors for all eight rock-physics theories (rows) across three velocity cases. Each curve is the wet-end-member thickness density $\varsigma_{\mathrm{wet}}(D_{\mathrm{water}})$ conditional on $S_w = 1$, with unit area, and all theories are drawn on a single common vertical scale, so peak heights are directly comparable across rows. The dry end-member contributes the remaining probability $1 - P_{\mathrm{wet}}$ as a point mass at $D_{\mathrm{water}} = 0$; this Dirac component is omitted from the plot, since rendering it on a density axis would produce a spike at zero that dominates the figure and obscures the wet-branch shape. The wet/dry split P_{wet} for each theory–velocity + + +

medium. Water vapor is excluded *a priori*: lithostatic pressure at mid-crustal depths exceeds the saturation vapor pressure of water at any plausible mid-crustal temperature below water's critical point ($T_c \approx 374°C$), so liquid and ice are the only physically admissible phases in this depth range. If mid-crustal temperatures are lower than current thermal models suggest, water could exist as ice rather than liquid at these depths. However, Manga and Wright (2021) show that the observed V_s is too low to be ice-saturated, an argument extended by Kilburn et al. (2022); together they indicate that ice-saturated rocks are inconsistent with the observed V_s, lending support to the liquid-water assumption adopted here.

Finally, the predominant reliance on the InSight mission as the source of Mars-specific seismic constraints introduces additional uncertainty (Golombek et al., 2020). The V_p and V_s estimates we test are all derived from InSight observations at a single landing-site region (Li et al., 2022; Wieczorek et al., 2022; Wright et al., 2024), and crustal thickness is constrained by InSight in combination with gravity and topography (Kilburn et al., 2022; Wright et al., 2024); the bulk density we adopt is obtained from gravity and topography rather than from seismic data directly (Wieczorek et al., 2022). Although these constraints are internally consistent, they sample only a single locality on Mars, and their applicability to the global Martian crust remains uncertain.

4. Conclusion

We extended the Bayesian inversion of Wright et al. (2024) by testing additional rock-physics configurations across three elastic parameter sets. We conclude that the presence of liquid water in the Mars mid-crust remains weakly constrained by existing data (Figs. 1–2): across three statistically indistinguishable velocity sets the inferred water content spans an order of magnitude, so how much water one infers is governed less by the data than by the adopted seismic inputs and the choice of rock-physics model. Among the rock-physics theories, HS with Hill mixing is the most robust to that choice, as it invokes no unconstrained crack aspect ratio; under the higher-velocity case ($V_p = 4.7$ km/s) this configuration indicates a negligible amount of crustal liquid water—a posterior with the majority of its thickness probability below 0.5 km (median ≈ 0.35 km). We present this as one defensible end of the inferred range rather than as a preferred velocity for the mid-crust, since the velocity sets themselves are measurements to be explained rather than competing values to be selected among. This range, like the inferred water content itself, remains conditioned on the adopted prior bounds (Supplementary Section S3). Stronger constraints would require tighter seismic inputs with broader applicability to the Mars mid-crust. Furthermore, while rock-physical models that better capture crack variability and anisotropy do exist, meaningfully applying their added complexity would require additional geophysical data, such as shear-wave splitting measurements to constrain anisotropy, that are not yet available.

CRediT authorship contribution statement

Mufan Zha: Writing – review & editing, Writing – original draft, Visualization, Software, Methodology, Formal analysis, Data curation, Conceptualization; **Per Avseth:** Conceptualization, Methodology, Writing – review & editing; **Paul Sava:** Conceptualization, Writing – review & editing, Supervision.

Declaration of generative AI and AI-assisted technologies in the manuscript preparation process

During manuscript preparation, the authors used ChatGPT (OpenAI, GPT-4) and Claude (Anthropic) for plot generation, debugging assistance, and language editing. These models were employed to refine wording and clarify technical explanations, after which all suggestions were critically evaluated and edited by the authors. The authors assume full responsibility for the content of the manuscript.

Declaration of competing interest

The authors declare no competing interest.

Acknowledgements

We thank the members of the Center for Wave Phenomena (CWP) at Colorado School of Mines for their constructive feedback during the development of this work. We acknowledge NASA, CNES, their partner agencies and institutions, and the operators of JPL, SISMOC, MSDS, IRIS-DMC, and PDS for providing InSight data. This research received no specific grant from any funding agency in the public, commercial, or not-for-profit sectors.

Data availability

Modeling codes are available at https://github.com/timzha-2000/mars_water for reproducibility. Data available in Table 2. Supplementary Sections S1– S3 (porosity/saturation distributions, convergence diagnostics, and prior-box sensitivity) are provided as Supplementary Material.

Supplementary material

Supplementary material associated with this article can be found in the online version at 10.1016/j.epsl.2026.120235.

References

Adam, L., Batzle, M., Lewallen, K., van Wijk, K., 2009. Seismic wave attenuation in carbonates. J. Geophys. Res.: Solid Earth 114, B06208.
Avseth, P., Millett, J., Jerram, D., Planke, S., Healy, D., 2020. Rock physics analysis of volcanic lava flows and hyaloclastites. In: 82nd EAGE Annual Conference & Exhibition.
Bernadet, J., Borisova, A., Guitreau, M., Safonov, O., Asimow, P., Nédelec, A., Bohrson, W., Kosova, S., de Parseval, P., 2025. Making continental crust on water-bearing terrestrial planets. Sci. Adv. 11, eads6746.
Berryman, J., 1980. Long-wavelength propagation in composite elastic media I. Spherical inclusions. J. Acoust. Soc. Am. 68, 1809–1819.
Berryman, J., 1992. Single-scattering approximations for coefficients in Biot's equations of poroelasticity. J. Acoust. Soc. Am. 91, 551–571.
Berryman, J., Pride, S., Wang, H., 2002. A differential scheme for elastic properties of rocks with dry or saturated cracks. Geophys. J. Int. 151, 597–611.
Biot, M., 1956. Theory of propagation of elastic waves in a fluid-saturated porous solid. II. Higher frequency range. J. Acoust. Soc. Am. 28, 179–191.
Carr, M., Head, J., 2010. Acquisition and history of water on Mars. In: Lakes on Mars, Vol. 1. Elsevier, pp. 31–67.
Carrasco, S., Knapmeyer-Endrun, B., Margerin, L., Xu, Z., Joshi, R., Schimmel, M., Stutzmann, E., Charalambous, C., Lognonné, P., Banerdt, W., 2023. Constraints for the Martian crustal structure from Rayleigh waves ellipticity of large seismic events. Geophys. Res. Lett. 50, e2023GL104816.
Clifford, S., Parker, T., 2001. The evolution of the Martian hydrosphere: implications for the fate of a primordial ocean and the current state of the northern plains. Icarus 154, 40–79.
Drilleau, M., Samuel, H., Garcia, R., Rivoldini, A., Perrin, C., et al., 2022. Marsquake locations and 1-D seismic models for Mars from insight data. J. Geophys. Res.: Planets 127, e2021JE007067.
Duran, C., Khan, A., Ceylan, S., Zenhäusern, G., Staehler, S., Clinton, J., Giardini, D., 2022. Seismology on Mars: an analysis of direct, reflected, and converted seismic body waves with implications for interior structure. Phys. Earth Planet. Inter. 325, 106851.
Foreman-Mackey, D., Hogg, D., Lang, D., Goodman, J., 2013. emcee: the MCMC hammer. Publ. Astron. Soc. Pac. 125, 306–312.
Gal, D., Dvorkin, J., Nur, A., 1998. A physical model for porosity reduction in sandstones. Geophysics 63, 454–459.
Gassmann, F., 1951. Elastic waves through a packing of spheres. Geophysics 16, 673–685.
Genova, A., Petricca, F., Andolfo, S., Gargiulo, A., Sulcanese, D., Mitri, G., Chiarolanza, G., 2024. Water ice concentration and distribution in the Martian south polar layered deposits constrained by the lateral variations of their bulk density. Icarus 414, 116025.
Golombek, M., Warner, N., Grant, J., Hauber, E., Ansan, V., Weitz, C., Williams, N., Charalambous, C., Wilson, S., DeMott, A., et al., 2020. Geology of the insight landing site on mars. Nat. Commun. 11, 1014.
Goodman, J., Weare, J., 2010. Ensemble samplers with affine invariance. Commun. Appl. Math. Comput. Sci. 5, 65–80.
Hashin, Z., Shtrikman, S., 1963. A variational approach to the theory of the elastic behaviour of multiphase materials. J. Mech. Phys. Solids 11, 127–140.
Hill, R., 1952. The elastic behaviour of a crystalline aggregate. Proc. Phys. Soc. A 65, 349–354.

Johnson, B., Milliken, R., Lewis, K., Collins, G., 2021. Impact generated porosity in Gale Crater and implications for the density of sedimentary rocks in lower Aeolis Mons. Icarus 366, 114539.
Joshi, R., Knapmeyer-Endrun, B., Mosegaard, K., Wieczorek, M., Igel, H., Christensen, U., Lognonné, P., 2023. Joint inversion of receiver functions and apparent incidence angles to determine the crustal structure of mars. Geophys. Res. Lett. 50, e2022GL100469.
Katayama, I., Akamatsu, Y., 2024. Seismic discontinuity in the Martian crust possibly caused by water-filled cracks. Geology 52, 939–942.
Kilburn, R., Dasent, J., Wright, V., Manga, M., 2022. Lithology, pore-filling media, and pore closure depth beneath insight on mars inferred from shear wave velocities. J. Geophys. Res.: Planets 127, e2022JE007539.
Kitamura, K., Ishikawa, M., 1998. Rock velocities at atmospheric pressure and room temperature in Tanzawa Plutonic rocks from central Japan. Mem. Natl. Inst. Polar Res. Spec. Issue 53, 192–202. https://nipr.repo.nii.ac.jp/records/2345.
Knapmeyer-Endrun, B., Adam, L., Carrasco, S., Golombek, M., Kim, D., Knapmeyer, M., Miljković, K., Plesa, A., Warner, N., Wieczorek, M., 2025. Porosity and hydrous alteration of the Martian crust from insight seismic data. Phys. Earth Planet. Inter. 366, 107383.
Knapmeyer-Endrun, B., Panning, M., Bissig, F., Joshi, R., Khan, A., Kim, D., Lekić, V., Tauzin, B., Tharimena, S., Plasman, M., et al., 2021. Thickness and structure of the Martian crust from insight seismic data. Science 373, 438–443.
Krasnopolsky, V., 2002. Mars' upper atmosphere and ionosphere at low, medium, and high solar activities: implications for evolution of water. J. Geophys. Res.: Planets 107, 1–11.
Kurokawa, H., Sato, M., Ushioda, M., Matsuyama, T., Moriwaki, R., Dohm, J., Usui, T., 2014. Evolution of water reservoirs on Mars: constraints from hydrogen isotopes in Martian meteorites. Earth Planet. Sci. Lett. 394, 179–185.
Kuster, G., Toksoz, M., 1974. Velocity and attenuation of seismic waves in two-phase media—Part I. Geophysics 39, 587–606.
Lalich, D., Hayes, A., Poggiali, V., 2022. Explaining bright radar reflections below the south pole of Mars without liquid water. Nat. Astron. 6, 1142–1146.
Lewis, K., Peters, S., Gonter, K., Morrison, S., Schmerr, N., Vasavada, A., Gabriel, T., 2019. A surface gravity traverse on Mars indicates low bedrock density at Gale Crater. Science 363, 535–537.
Li, J., Beghein, C., McLennan, S., Horleston, A., Charalambous, C., Huang, Q., et al., 2022. Constraints on the Martian crust away from the insight landing site. Nat. Commun. 13, 7950.
Manga, M., Wright, V., 2021. No cryosphere-confined aquifer below insight on mars. Geophys. Res. Lett. 48, e2021GL093127.
Mavko, G., Mukerji, T., Dvorkin, J., 2020. The Rock Physics Handbook: Tools for Seismic Analysis of Porous Media. Cambridge University Press. 3rd edition.
McSween, H. Y.J., Taylor, G.J., Wyatt, M.B., 2009. Elemental composition of the Martian crust. Science 324, 736–739.
McSween Jr, H., 2015. Petrology on Mars. Am. Mineral. 100, 2380–2395.
Nazari-Sharabian, M., Aghababaei, M., Karakouzian, M., Karami, M., 2020. Water on Mars—a literature review. Galaxies 8, 40.
Orosei, R., Lauro, S., Pettinelli, E., Cicchetti, A., Coradini, M., Cosciotti, B., Di Paolo, F., Flamini, E., Mattei, E., Pajola, M., et al., 2018. Radar evidence of subglacial liquid water on Mars. Science 361, 490–493.
Reuss, A., 1929. Berechnung der Fließgrenze Von Mischkristallen Auf Grund Der Plastizitätsbedingung für Einkristalle. ZAMM-J. Appl. Math. Mech./Z. Angew. Math. Mech. 9, 49–58.
Scheller, E., Ehlmann, B., Hu, R., Adams, D., Yung, Y., 2021. Long-term drying of Mars by sequestration of ocean-scale volumes of water in the Crust. Science 372, 56–62.
Sprunt, E., Nur, A., 1977. Destruction of porosity through pressure solution. Geophysics 42, 726–741.
Squyres, S., 1984. The history of water on Mars. Annu. Rev. Earth Planet. Sci. 12, 83.
Tarantola, A., 2005. Inverse Problem Theory and Methods for Model Parameter Estimation. Vol. 89 of *Other Titles in Applied Mathematics*. Society for Industrial and Applied Mathematics (SIAM).
Voigt, W., 1910. Lehrbuch der Kristallphysik:(Mit Ausschluss der Kristalloptik). Vol. 34. BG Teubner.
Wernicke, L., Jakosky, B., 2021. Martian hydrated minerals: a significant water sink. J. Geophys. Res.: Planets 126, e2019JE006351.
Wieczorek, M., Broquet, A., McLennan, S., Rivoldini, A., Golombek, M., Antonangeli, D., Beghein, C., Giardini, D., Gudkova, T., Gyalay, S., et al., 2022. Insight constraints on the global character of the Martian crust. J. Geophys. Res.: Planets 127, e2022JE007298.
Wood, A.B., 1955. A textbook of sound. 3rd ed., G. Bell and Sons, London.
Wright, V., Morzfeld, M., Manga, M., 2024. Liquid water in the Martian mid-crust. Proc. Natl. Acad. Sci. U. S. A. 121, e2409983121.
Wright, V., Morzfeld, M., Manga, M., 2025. Reply to xiao et al.: a wet or dry Martian Mid-Crust, that is only part of the question. Proc. Natl. Acad. Sci. 122, e2505168122.
Xiao, W., Pan, L., Wang, Y., Li, J., 2025. Liquid water might not be the only answer: evaluating pore-filling materials in the Martian Crust. Proc. Natl. Acad. Sci. 122, e2503071122.